

ECOLOGY

Cryptic coral diversity is associated with symbioses, physiology, and response to thermal challenge

Hannah E. Aichelman^{1*}, Brooke E. Benson^{1,2,†}, Kelly Gomez-Campo³, M. Isabel Martinez-Rugiero³, James E. Fifer¹, Laura Tsang¹, Annabel M. Hughes¹, Colleen B. Bove^{1,‡}, Olivia C. Nieves¹, Alyssa M. Pereslete¹, Darren Stanizzi¹, Nicola G. Kriefall^{1,§}, Justin H. Baumann^{2,¶}, John P. Rippe², Plinio Gondola⁴, Karl D. Castillo^{2,5}, Sarah W. Davies^{1*}

Coral persistence in the Anthropocene depends on interactions among holobiont partners (coral animals and microbial symbionts) and their environment. Cryptic coral lineages—genetically distinct yet morphologically similar groups—are critically important as they often exhibit functional diversity relevant to thermal tolerance. In addition, environmental parameters such as thermal variability may promote tolerance, but how variability interacts with holobiont partners to shape responses to thermal challenge remains unclear. Here, we identified three cryptic lineages of *Siderastrea siderea* in Bocas del Toro, Panamá that differ in distributions across inshore and offshore reefs, microbial associations, phenotypic traits of holobiont partners (i.e., phenomes), and skeletal morphologies. A thermal variability experiment failed to increase thermal tolerance, but subsequent thermal challenge and recovery revealed that one lineage maintained elevated energetic reserves, photochemical efficiency, and growth. Last, coral cores highlighted that this lineage also exhibited greater growth historically. Functional variation among cryptic lineages highlights their importance in predicting coral reef responses to climate change.

INTRODUCTION

Climate change is altering environments at unprecedented rates, resulting in warmer and increasingly variable conditions with more extreme events (1). An organism's response to such rapid changes [e.g., through shifts in thermal limits; (2)] is influenced by their genetic background, environmental history, and interactions between these two forces [GxE; (2, 3)]. Understanding and predicting the relative importance of these factors on fitness are fundamental as environments continue to change, species ranges shift, and localized extinctions occur (1, 2).

Coral reefs represent one of the most productive and economically valuable ecosystems (4, 5) threatened by global (e.g., warming and acidification) and local (e.g., nutrient pollution and overfishing) stressors (6). These stressors have increased the frequency and severity of coral bleaching—loss of the coral's obligate symbiotic algae (7)—which is projected to worsen under current emissions trajectories (8). However, reef environments are not changing homogeneously, and although our understanding of which reefs and species are more bleaching resistant is advancing (9), predicting their future remains challenging due to complexities governing coral resilience, including environmental variation, host genetics, and associations with diverse algal and bacterial symbionts (10).

Coral “holobionts” encompass complex symbioses among coral hosts, algal symbionts (Symbiodiniaceae), and a diverse array of microorganisms, all interacting to shape aggregated holobiont phenotypes

(i.e., phenomes). Each member of the holobiont contributes to coral bleaching heterogeneity, including genetic variation of the host (11), algal symbiont communities (12), and bacterial communities (13). For coral hosts, genomic sequencing has revealed an unexpected level of cryptic diversity, including cryptic lineages [i.e., distinct genetic clusters previously characterized as one species; (14, 15)]. These lineages can also interact with a diversity of holobiont members to produce functionally distinct phenotypes. For example, a lineage in the *Acropora hyacinthus* species complex more frequently hosts *Durussdinium* algae and exhibits higher thermal tolerance, although it coexists with other lineages on the same reef (16). Together, interactions among these cryptic lineages and holobiont members likely play a role in determining bleaching outcomes.

In addition to holobiont genetic variation, environmental heterogeneity can influence coral bleaching patterns (17) and a growing body of literature links coral thermotolerance to high frequency temperature variability, also termed diel thermal variability (DTV) [e.g., (18, 19)]. DTV is theorized to “prime” [i.e., beneficial acclimation hypothesis; (20)] organisms to more effectively respond to and recover from heat stress (21–23). However, DTV is correlated with other environmental parameters that can also produce beneficial acclimatory effects [e.g., light and flow; (24, 25)], and it remains unclear whether this variability facilitates thermotolerance via priming and/or whether environmental selection in high DTV environments is selecting for more thermally tolerant individuals. For example, cryptic coral lineages are known to exhibit divergent spatial distributions across depths (26), which likely involves adaptations in photosynthetic pigment concentrations and skeletal traits that can have important effects on light-harvesting potential (27, 28). In addition, lineages and their algal symbionts (29) have been shown to segregate across inshore–offshore gradients, where offshore habitats experience lower turbidity, higher flow, and more stable temperatures relative to inshore habitats [e.g., (30)]. Together, these patterns of complex environmental heterogeneity likely produce adaptive phenotypes through a combination of acclimation and selection for unique holobiont combinations.

¹Department of Biology, Boston University, Boston, MA, USA. ²Department of Earth, Marine, and Environmental Sciences, University of North Carolina at Chapel Hill, Chapel Hill, NC, USA. ³Department of Biology, Pennsylvania State University, State College, PA, USA. ⁴Smithsonian Tropical Research Institution, Bocas del Toro, Panamá. ⁵Environment, Ecology, and Energy Program, University of North Carolina at Chapel Hill, Chapel Hill, NC, USA.

*Corresponding author. Email: haich@bu.edu (H.E.A.); daviessw@bu.edu (S.W.D.)

†Present address: University of California, Davis, Davis, CA, USA.

‡Present address: Ursinus College, Collegeville, PA, USA.

§Present address: University of Hawai'i at Mānoa, Honolulu, HI, USA.

¶Present address: Bates College, Lewiston, ME, USA.

To investigate the influence of coral holobiont diversity and environmental history on coral phenomes, we characterized holobiont genetic diversity of the reef-building coral *Siderastrea siderea* from three inshore and three offshore sites in the Bocas del Toro reef complex (BTRC), Panamá. We found three cryptic lineages with unique symbiotic associations that differed in their distributions across the seascape, as well as distinct baseline phenomes and skeletal morphology. Next, we conducted a 50-day DTV experiment, followed by thermal challenge and recovery, to test the hypothesis that exposure to DTV would increase coral resistance to thermal challenge. In contrast to our hypothesis, we found that cryptic lineages differed in their response to thermal challenge, whereas the effect of experimental DTV treatment was minimal beyond promoting growth. Lineages also differed in their growth, especially under thermal challenge. To determine whether these growth differences between lineages were conserved in situ, we used coral cores to contrast long-term growth trajectories between lineages. We found that these records were consistent with experimental patterns, with lineages differing in skeletal density and linear extension rates. Together, these data showcase the strong influence that cryptic lineages have in shaping coral distributions, symbioses, thermotolerance, and growth. Failure to appreciate this genetic diversity will ultimately lead to challenges when predicting coral responses to climate change.

RESULTS

Three lineages of *S. siderea* with distinct distributions and symbioses found in Bocas del Toro

This study focused on the ubiquitous Caribbean reef-building coral, *S. siderea*, collected primarily from six sites in the BTRC, Panamá across inshore [Punta Donato (PD), STRI Point (SP), and Cristobal Island (CI)] and offshore [Bastimentos North (BN), Bastimentos South (BS), and Cayo de Agua (CA)] sites (Fig. 1A, $N = 9$ corals per site; table S1A). Corals from an additional inshore [Punta Laurel (PL)] and offshore [Drago Mar (DM)] site were included for historical growth data (Fig. 1A), which are described below. 2b-RAD sequencing (2b-RADseq) genotyping was conducted on 54 coral colonies. Admixture ancestry of individuals across sites (Fig. 1A and fig. S1A), principal coordinate analysis (PCoA) based on the identity by state (IBS) matrix (Fig. 1A), and hierarchical clustering of pairwise IBS values (fig. S1, C and D) supported the presence of three distinct coral host genetic clusters (hereafter referred to as cryptic lineages L1, L2, and L3) across the BTRC. Pairwise global weighted F_{ST} values revealed high divergence between these genetic clusters (L1 versus L2 = 0.17, L1 versus L3 = 0.18, L2 versus L3 = 0.12; Fig. 1A), suggesting that they represent three cryptic lineages of a *S. siderea* species complex. Cryptic lineages differed in their spatial distributions across the BTRC, with more L1 individuals sampled at offshore sites (83%; 24/29 offshore/total L1 individuals) and more L2 individuals sampled at inshore sites (94%; 17/18 inshore/total L2 individuals; $X^2 = 23.57$, $P < 0.001$). Although temperature logger data are not available for all sites where corals were collected, mean DTV (\pm SE) at sites where L2 dominates (PD = $0.71^\circ \pm 0.01^\circ\text{C}$ and SP = $0.54^\circ \pm 0.01^\circ\text{C}$) is significantly lower than DTV at sites where L1 was found (CA = $0.98^\circ \pm 0.02^\circ\text{C}$ and CI = $1.17^\circ \pm 0.03^\circ\text{C}$; Fig. 1B; tables S1 and S2; all $P < 0.0001$).

L3 was the least abundant lineage, with only three individuals observed at SP (Fig. 1A). CI is the only site where two lineages were sampled in equal proportion ($n = 4$ L1 and $n = 4$ L2; Fig. 1A). ADMIXTURE

results at $K = 2$ suggest that L3 individuals are of mixed ancestry between L1 and L2; however, L3 fully resolves as a distinct lineage at $K = 3$ (fig. S1A). Cryptic lineages had low admixture, and the individual with the most admixture had $<5\%$ assigned to a second ancestral population. To provide support for L3 being a distinct lineage and not an artifact of genetically related individuals [e.g., (31)], we computed pairwise relatedness values within each cryptic lineage (fig. S1B). Results support L3 being a distinct genetic lineage; however, given the small sample size for L3, these individuals were excluded from all downstream analyses. Additional work will be necessary to fully describe L3 and characterize its evolutionary history with L1 and L2.

16S metabarcoding of the same coral colonies determined that bacterial communities were significantly different between L1 and L2 (Fig. 1C; ADONIS $P = 0.003$; table S3) when sampled before experimental acclimation (hereafter termed “baseline”; full experimental design detailed in fig. S2). No differences were observed for any bacterial community alpha diversity metrics [amplicon sequence variant (ASV) richness, Shannon’s index, Simpson’s index, and evenness] across host lineages for baseline samples (fig. S3 and table S4).

ITS2 metabarcoding revealed that, when Symbiodiniaceae communities were aggregated by the majority ITS2 sequence assigned by SymPortal (32), 19 Symbiodiniaceae ITS2 defining intragenomic variants (DIVs) matched the C1 majority ITS2 sequence (*Cladocopium goreauii*), 2 DIVs matched C3, 9 DIVs matched D1 (*Durusdinium trenchii*), and 1 DIV matched each of the A4, A4z, B19, B5, and C3af majority ITS2 sequences. At baseline, significantly more L1 (72.4%) hosted $>50\%$ relative abundance of *D. trenchii* relative to L2 (22.2%) (Kruskal-Wallis $X^2 = 12.68$, $P = 0.0004$; Fig. 1D). When only considering corals from the site where an equal proportion of L1 and L2 individuals were collected (CI) at baseline, differences in the relative abundance of *D. trenchii* between lineages were no longer significant, with 25% of L1 and 75% of L2 hosting $>50\%$ relative abundance of *D. trenchii* (Kruskal-Wallis $X^2 = 0.788$, $P = 0.37$).

Cryptic host lineages exhibited distinct phenomes and skeleton morphologies

Corals of L1 and L2 ancestry exhibited distinct baseline holobiont phenomes [Fig. 2A; ADONIS $P < 0.0001$, partial omega-square (ω^2) = 0.14; table S5]. Lineages were distinguished by the first principal component (PC), with loadings for energy reserves (symbiont density, host and symbiont carbohydrate, chlorophyll a, and protein) positively correlated with L1 (Fig. 2A). Comparing holobiont phenomes (Fig. 2A) with individual physiology results (fig. S4 and table S6) supports L1 having significantly greater total protein, total host and symbiont carbohydrates, chlorophyll a, and symbiont density relative to L2 at baseline.

Corals of L1 and L2 ancestry exhibited distinct skeleton morphologies at baseline (Fig. 2B). Principal components analysis (PCA) of all skeletal parameters showcased that combined skeleton morphologies were significantly different across lineages (Fig. 2B; ADONIS $P = 0.0007$, $\omega^2 = 0.18$; table S7). Lineages were distinguished by the first PC, with loadings for septal length, distance between corallites, calyx diameter, corallite area, and light enhancement factor (LEF) positively correlated with L2 (Fig. 2B). L2 had larger corallite area when compared to L1 (58% larger; $P < 0.0001$; fig. S5A and table S8). This pattern was consistent even at CI where L1 and L2 co-occur, with L2 ($N = 4$) maintaining larger corallites than L1 (80% larger; $N = 4$; fig. S5B; $P = 0.001$;

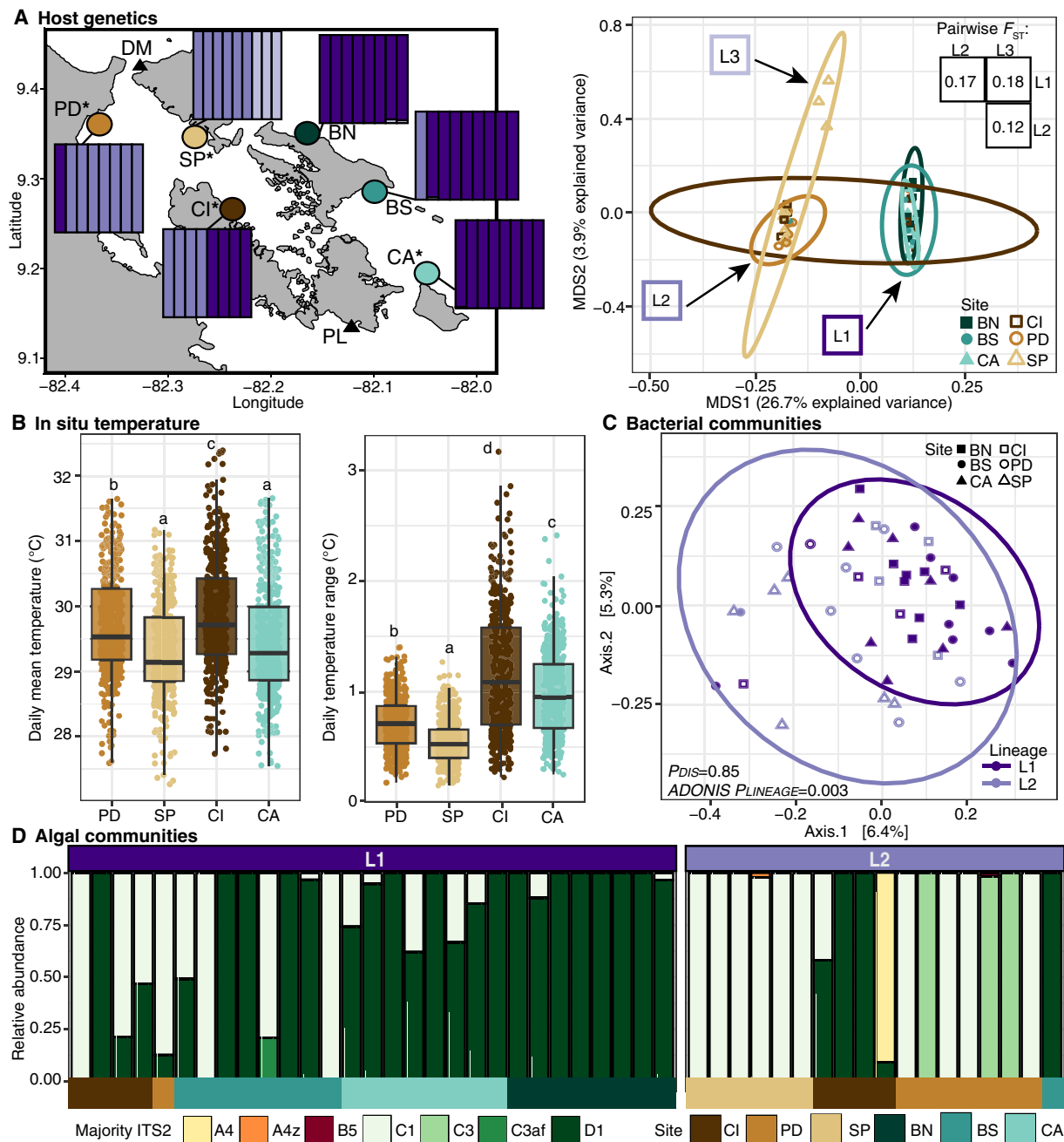


Fig. 1. Cryptic lineages exhibit distinct symbioses. (A) Map (left) indicating eight sites across the BTRC in Panamá where *S. siderea* were collected. Primary sites include three inshore (brown shades: PD, Punta Donato; SP, STRI Point; and CI, Cristobal Island) and three offshore (green shades: BN, Bastimentos North; BS, Bastimentos South; and CA, Cayo de Agua) sites. Coral cores were taken from these six sites plus an additional two sites (black triangles: inshore: Punta Laurel, PL; offshore: Drago Mar, DM). Asterisks indicate sites where temperature loggers were recovered. ADMIXTURE results from 2b-RADseq data for $K = 3$ are grouped by collection site. Columns represent an individual, and the bar color shows assignment to one of three ancestral populations (L1, dark purple; L2, medium purple; and L3, light purple). PCoA (right) illustrating clustering of lineages across collection sites ($N = 50$ individuals). Shapes and colors distinguish sites. Inset shows pairwise F_{ST} values between lineages. (B) Daily mean temperature (left) and daily temperature range (right) recorded using HOBO loggers for ~1 year prior to coral collection (10 June 2015 to 14 August 2016). Distinct letters indicate significant differences in temperature parameters from ANOVA and Tukey's post hoc tests (table S2; $N = 431$ per site). (C) Bray-Curtis dissimilarity PCoA of coral bacterial communities using all ASVs from cleaned and rarefied 16S metabarcoding data. Ellipses represent 95% confidence intervals, *ADONIS* P values indicate significant community differences, and P_{DIS} values compare dispersion across lineages (table S3; L1: $N = 29$, L2: $N = 18$). (D) Bar plots of Symbiodiniaceae majority ITS2 sequence relative abundance data, colored by majority ITS2 type. Each column of the bar plot represents a host colony, with color blocks representing site of origin, as in (A).

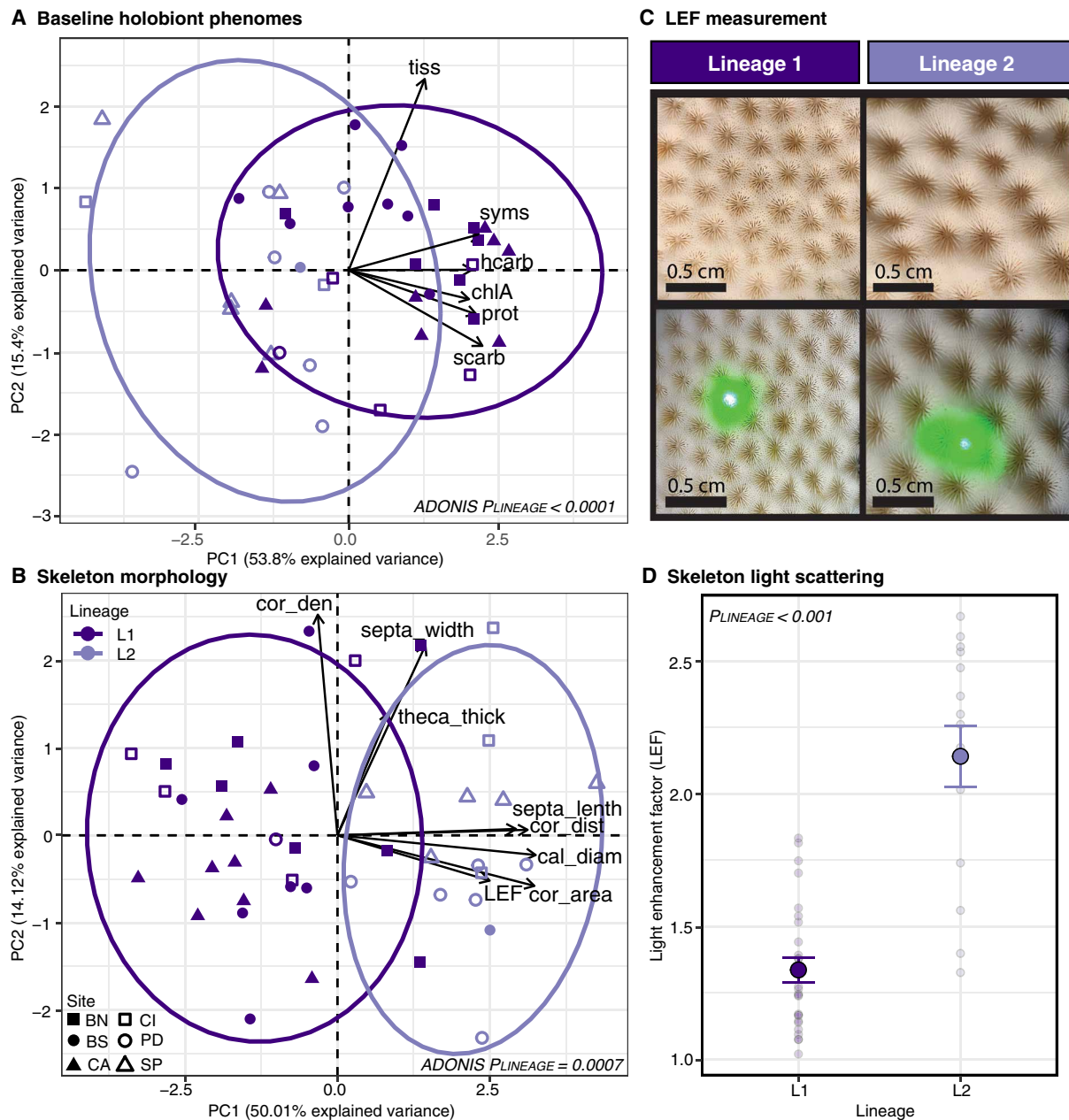


Fig. 2. Phenomes and skeleton morphology differ between cryptic host lineages. (A) PCA of log-transformed holobiont phenomes showcasing baseline differences between L1 and L2. Phenotypes include tissue thickness (tiss; mm), symbiont density (syms; cells cm⁻²), host and symbiont carbohydrate (hcarb and scarb, respectively; mg cm⁻²), chlorophyll a (chIA; μg cm⁻²), and total protein (prot; mg cm⁻²). *P* value indicates a significant difference in holobiont phenomes determined from a PERMANOVA, only individuals with data for all phenotypes were included (L1: *N* = 28, L2: *N* = 14; table S5). (B) PCA of log-transformed coral skeleton morphology sampled at baseline. Phenotypes include corallite area (cor_area; cm⁻²), corallite density (cor_den; # cm⁻²), septal width (septa_width; cm), theca thickness (theca_thick; cm), distance between corallites (cor_dist; cm), septal length (septa_lenth; cm), calyx diameter (cal_diam; cm), and LEF. Statistical analyses as in (A) (L1: *N* = 27, L2: *N* = 15; table S7). (C) Top: photos of representative skeletons from L1 (left) and L2 (right). Bottom: photos of LEF measurements, illustrating lineage differences in the ability for the skeleton to enhance the light field for algal photosynthesis. (D) Lineage differences in skeleton LEF (L1: *N* = 27, L2: *N* = 15). *P* value indicates significant difference in LEF (table S8). Large points represent mean LEF ± SE for each lineage, and smaller points represent an individual fragment's LEF.

table S8). This variation in skeletal morphology contributed to a significantly higher LEF in L2 compared to L1 (Fig. 2, C and D; *P* < 0.0001; table S8), indicating an increased ability of L2 skeletons to enhance the light field for algal photosynthesis. Similarly, L2 maintained significantly greater LEF at CI, where lineages co-occur (fig. S5C; *P* = 0.04; table S8).

DTV influenced growth and bacterial communities, but host lineages shaped algal symbioses

To explore how lineages collected from sites across the BTRC respond to differences in DTV, we conducted a 50-day DTV experiment where corals were exposed to either no variability control conditions (average daily mean ± average daily variability = 29.5° ± 0.4°C)

or DTV ($29.4^{\circ} \pm 2.9^{\circ}\text{C}$; treatment temperatures summarized in table S1B). Buoyant weight assessments showed an effect of DTV on growth, with corals exposed to DTV growing faster than control corals (32.9% increase; Fig. 3A; $P = 0.02$; table S9). In addition, under DTV, L1 growth trended toward being faster than L2 (36.9% increase; Fig. 3A; $P = 0.08$).

At the end of the DTV experiment, coral fragments were subsampled for 16S and ITS2 metabarcoding to explore how DTV

modulated symbioses. 16S data showed that bacterial communities were no longer structured by host lineage (*ADONIS* $P = 0.11$; fig. S6A). However, communities in DTV were distinct from those in control (*ADONIS* $P = 0.045$; fig. S6B and table S3). In addition, ASV richness was higher in control corals compared to corals exposed to DTV (fig. S6I; $P = 0.023$; table S4). No other differences were observed for any bacterial community diversity metrics (ASV richness, Shannon's index, Simpson's index, and evenness) across host

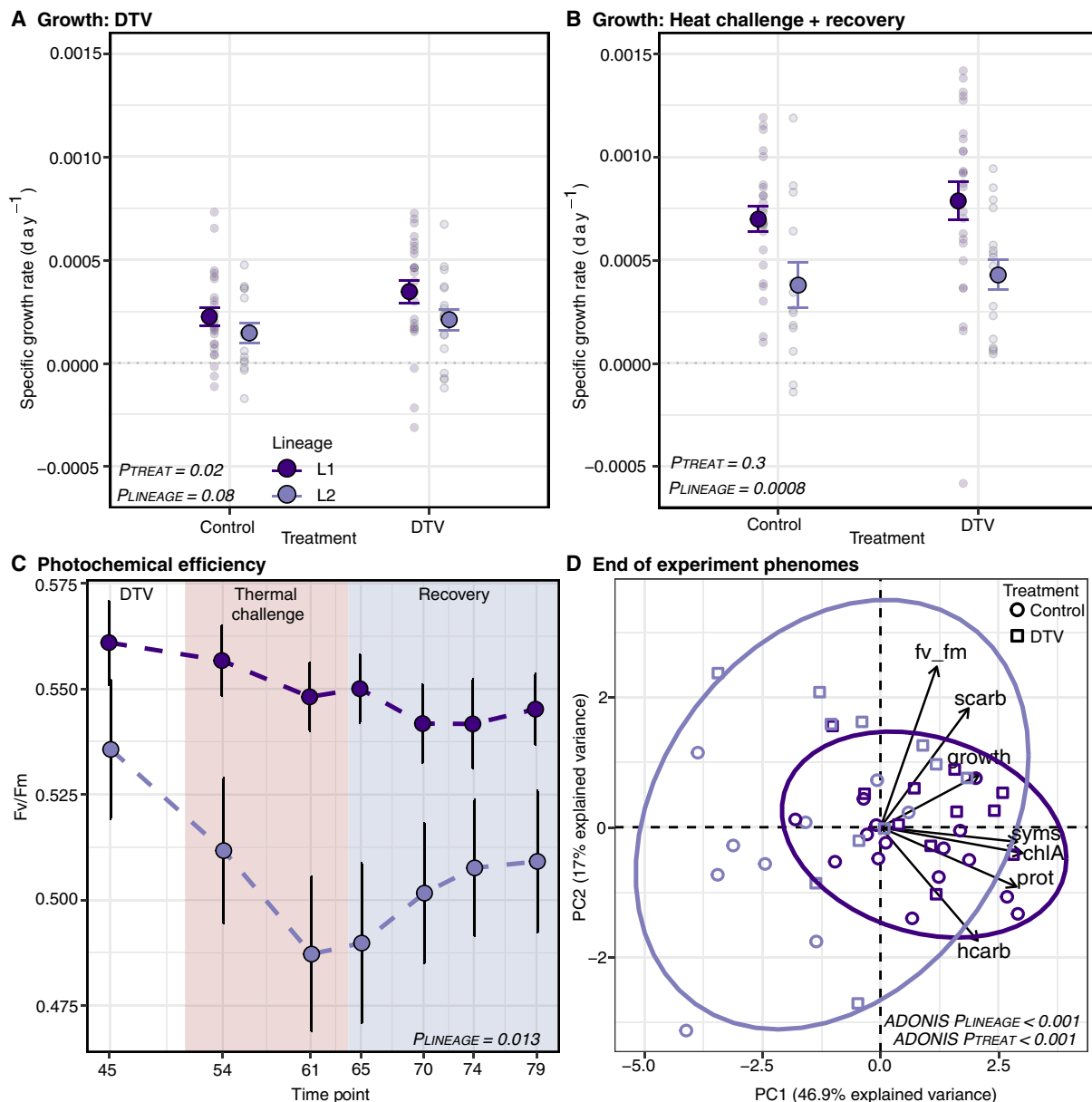


Fig. 3. Lineage responses to DTV and thermal challenge. Specific growth rate day^{-1} between DTV treatments showing lineage growth throughout the DTV experiment (A) and thermal challenge and recovery (B). Large points represent mean growth \pm SE for each lineage, and smaller points represent an individual fragment's growth [(A): Control: L1 $N = 24$, L2 $N = 15$, DTV: L1 $N = 25$, L2 $N = 18$; (B): Control: L1 $N = 24$, L2 $N = 13$, DTV: L1 $N = 25$, L2 $N = 17$]. P values indicate significant differences in growth (table S9). (C) Photochemical efficiency of photosystem II (Fv/Fm) across seven time points including the end of DTV treatment and throughout heat stress (red shaded) and recovery (blue shaded). Points represent mean Fv/Fm \pm SE for each lineage (L1: $N = 32$; L2: $N = 21$; table S10). (D) PCA of log-transformed holobiont phenomes at the end of the experiment. Phenotypes include specific growth rate through 50 days in DTV (growth), total protein (prot; mg cm^{-2}), host and symbiont carbohydrate (hcarb and scarb, respectively; mg cm^{-2}), chlorophyll a (chlA; mg cm^{-2}), symbiont density (syms; cells cm^{-2}), and Fv/Fm. Only individuals with data for all phenotypes were included (L1: $N = 26$, L2: $N = 20$), and P values indicate significant differences in holobiont phenomes determined from PERMANOVA (table S5).

lineage or variability treatment (fig. S6, C to J, and table S4). ITS2 data showed that Symbiodiniaceae communities continued to be differentiated by cryptic host lineage after 50 days of DTV (fig. S7) with 49.1% of L1 hosting >50% relative abundance of *D. trenchii* compared to 12.9% in L2 (Kruskal-Wallis $X^2 = 16.82$, $P < 0.0001$).

Host lineage, not DTV, drove responses to thermal challenge, but both shaped holobiont phenomes

To explore how DTV influenced response to thermal challenge and recovery, after 50 days of DTV, all corals were exposed to a 2-week thermal challenge followed by a 2-week recovery. Buoyant weights showed that growth benefits afforded from exposure to variability were not sustained and prior exposure to DTV failed to rescue growth during the thermal challenge and recovery periods (Fig. 3B; $P = 0.3$; table S9). However, L1 grew significantly faster than L2 during these periods (45.4% increase; Fig. 3B; $P = 0.0008$; table S9) and L1 maintained higher photochemical efficiency of photosystem II (Fv/Fm) than L2 throughout thermal challenge and recovery (7.8% increase; Fig. 3C; $P = 0.013$; table S10). Prior exposure to DTV did not have a significant effect on Fv/Fm during thermal challenge and recovery (Fig. 3C; $P = 0.21$; table S10). Together, these data suggest that lineages exhibit divergent responses to thermal challenge.

At the end of the thermal challenge and recovery periods, coral fragments were flash frozen and holobiont phenomes were examined. Similar to baseline conditions (Fig. 2A), host lineages maintained distinct holobiont phenomes at the end of the experiment (Fig. 3D; *ADONIS* $P < 0.001$; $\omega^2 = 0.201$; table S5), with loadings for host and symbiont energy reserves, symbiont density, and chlorophyll a positively correlated with L1. Individual physiology metrics (fig. S4 and table S6) demonstrate that L1 maintained significantly more total protein, total host carbohydrates, chlorophyll a, and symbiont density than L2 at the end of the experiment. In addition, DTV treatment influenced holobiont phenomes, with control corals

distinguishing from corals exposed to variability (Fig. 3D; *ADONIS* $P < 0.001$; $\omega^2 = 0.19$; table S5). Individual physiology metrics suggest that this difference was driven by greater symbiont density and symbiont carbohydrates, but reduced host carbohydrates, in corals exposed to DTV relative to control (fig. S4).

It is important to note that, whereas a coral's dominant symbiont type (>50% relative read abundance of an ITS2 sequence) does appear to influence physiology [i.e., growth (fig. S8, A and B) and Fv/Fm (fig. S8C)], our ability to make statistically robust comparisons of how dominant symbiont type and cryptic lineage interact to influence coral physiology is limited by sample size in this dataset.

Host lineages exhibited distinct patterns of historical growth

To explore whether the lineage differences in growth observed under experimental conditions are conserved in situ, we assessed patterns of annual growth from coral cores between 1980 and 2014 that were genotyped via 2b-RADseq as described above (L1: $N = 16$, L2: $N = 8$ cores). L1 maintained significantly higher linear extension ($P = 0.03$; Fig. 4A) and lower skeletal density ($P = 0.004$; Fig. 4B) compared to L2 (table S11). Although L1 cores trended toward greater calcification than L2, these differences were not statistically significant ($P = 0.11$; Fig. 4C; table S11). These patterns were consistent when considering linear extension, skeletal density, and calcification data across the entire history of the coral cores, with the longest record being 1880 to 2014 (fig. S9 and table S11). Although both annual mean and annual summer mean temperatures have increased in the BTRC over the lifetime of the coral cores analyzed (fig. S10, A and B; $P < 0.001$; table S12), calcification was not significantly influenced by temperature across any time interval (fig. S10, C to F, and table S13). However, L1 maintained significantly greater calcification across both annual mean and annual summer mean temperatures for both time intervals considered (all $P < 0.001$; fig. S10, C to F, and table S13).

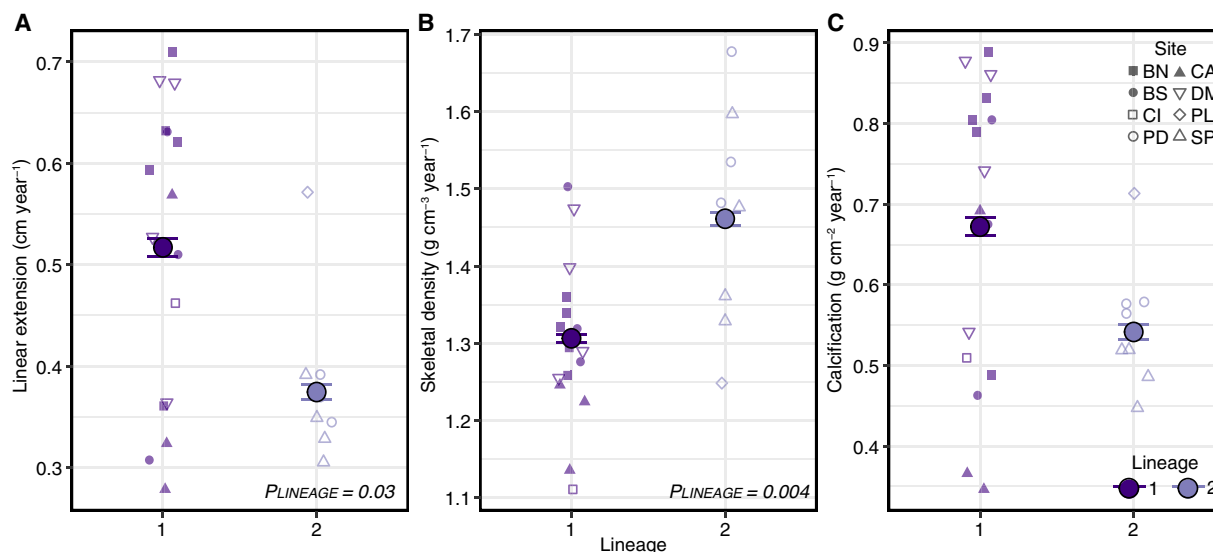


Fig. 4. Cryptic host lineages differ in historical growth. Linear extension (A), skeletal density (B), and calcification (C) across cryptic host lineages. For all panels, large points represent the mean \pm SE of each metric and smaller points represent an individual coral core. Shape of the smaller points represents the site of origin for that core (offshore: BN, Bastimentos North; BS, Bastimentos South; CA, Cayo de Agua, and DM, Drago Mar; inshore: PD, Punta Donato; SP, STRI Point; CI, Cristobal Island; and PL, Punta Laurel). Only data in the interval of 1980 to 2014 are included here ($N = 16$ L1 cores, $N = 8$ L2 cores; table S11).

DISCUSSION

Understanding how holobiont diversity is partitioned across the seascape is critical to predicting coral responses to climate change (11, 12). Here, we identified three cryptic host lineages (L1, L2, and L3) in a *S. siderea* species complex across the BTRC that varied in baseline phenotypes including algal and bacterial symbiont communities, energetic reserves, and skeletal morphology relevant to their in situ light environments. In addition, L1 corals maintained elevated energetic reserves throughout a mesocosm experiment, as well as elevated photochemical efficiency and growth throughout subsequent thermal challenge and recovery. Last, coral core data sampled from lineages across the BTRC demonstrated that these distinct growth patterns observed between lineages under experimental conditions were consistent with patterns of historical growth.

This work builds on the growing evidence for widespread cryptic diversity in corals (15), which has been detected at large [e.g., archipelago-wide; (33)] and small spatial scales, including within reefs in Puerto Rico (26), the Florida Keys (34), and American Samoa (16). Depth has emerged as a common driver of lineage differentiation in corals, with relevant abiotic factors including temperature, seawater optical properties (26, 34), and small-scale current patterns (35). Cryptic lineages have also been shown to exhibit divergence in ecologically relevant traits. For example, sympatric lineages of the *Pachyseris speciosa* species complex differ in skeletal morphology and holobiont physiology (27). In addition, lineages of *Porites* around Kiritimati exhibited differential mortality rates in response to a marine heat wave (36). Across larger spatial scales, only one of three *A. hyacinthus* cryptic lineages was able to occupy habitats along a range expansion front in Japan, which was attributed to divergence at loci associated with adaptation to temperate, seasonally fluctuating environments (33). Thermal variability has also been associated with differential distributions of *A. hyacinthus* cryptic lineages that exhibit distinct thermal tolerances in American Samoa (16, 37). Here, we build on the emerging understanding of cryptic coral diversity and provide an in-depth analysis of functional variation among lineages. Specifically, we find that cryptic lineages vary in their distributions across sites that differ in thermal variability, exhibit distinct and ecologically relevant phenomes (i.e., energetic reserves, skeletal morphologies, and growth) including responses to thermal challenge, and differ in patterns of historical growth.

We find evidence for environmental structuring of lineages and that unique skeleton morphologies could contribute to their success in these distinct environments. The cryptic host lineages identified here were structured across an inshore to offshore gradient in the BTRC, with L2 and L3 more prevalent inside Bahia Almirante (inshore), and L1 more prevalent outside the bay (offshore). Inshore BTRC sites are characterized by limited influence from the open ocean, riverine inputs that deliver nutrients, agricultural runoff and sewage to the bay, higher turbidity, and, most recently, hypoxic events that have altered coral communities (38, 39). We find evidence that lineages exhibit unique skeleton morphologies that could contribute to their success in these distinct environments. Namely, L2 skeleton morphology suggests that this lineage is better adapted to the low light environments of inshore BTRC to promote algal photosynthesis. The ability of L2 skeletons to better amplify incoming light could also explain its lower symbiont densities and chlorophyll a concentrations compared to L1, which would serve as a mechanism to reduce pigment packing while “sensing more light” (28, 40). These skeleton morphology differences persisted even when lineages coexisted in the same environment (CI), which

suggests a genetic basis for this trait. Future explorations of this system would benefit from collecting precise colony depths in addition to diffuse attenuation coefficients for downwelling irradiance (K_d) from each site to link in situ light environments with cryptic lineage assignment. This information, along with additional optical traits of the coral holobiont, particularly metrics taken with intact tissue, would provide more detailed information on how seawater optical properties drive lineage distributions in the BTRC [e.g., (41)].

These cryptic lineages not only occupied distinct habitats, but they also exhibited unique symbioses. L1 and L2 hosted distinct communities of bacterial symbionts at baseline; however, these differences did not persist after a 50-day DTV treatment. Instead, bacterial communities of corals exposed to variability were distinct from corals under control conditions. Although previous work has highlighted that bacterial communities can contribute to coral thermal tolerance [e.g., (13)], this does not seem to be the main driver here given that we observed thermal tolerance differences among corals with similar bacterial communities. In contrast, algal communities were strongly structured by lineage, with L1 associating with higher proportions of *D. trenchii* and hosting a unique *Cladocopium* (C3) DIV. Increased *D. trenchii* in L1 could contribute to their elevated Fv/Fm throughout thermal challenge relative to L2 as *D. trenchii* has been shown to confer thermal tolerance to some hosts [e.g., (12, 42)]. Rose *et al.* (16) also demonstrated that a more bleaching-resistant *A. hyacinthus* cryptic lineage hosted greater proportions of *D. trenchii*. Here, although some L2 colonies were dominated by *D. trenchii*, this only occurred in low frequencies at sites where both L1 and L2 were sampled (CI and BS). L2 appeared to show the greatest thermal resistance when it associated with C1; however, more statistically robust explorations of this pattern were limited by sample size. Additional sampling will be needed to better characterize the importance of these less common cryptic host lineage–symbiont associations on holobiont phenomes, growth, and thermal responses. Regardless, we posit that the elevated LEF of L2 skeletons coupled with their acclimation to lower light environments of inshore BTRC and lower symbiont densities could have led to reduced Fv/Fm during thermal challenge. Future work investigating the impact of acclimation to different light levels on heat tolerance in these lineages is warranted. In addition, as coral bacterial communities are strongly influenced by their host traits and environment (43), more thorough sampling across sites, cryptic lineages, and regions within a coral colony [e.g., (44)] will be necessary to better identify any lineage-specific bacterial taxa.

We initially hypothesized that DTV would shape coral phenomes to increase thermal resilience [e.g., (18, 21, 23, 45)]. Although an effect of experimental DTV on holobiont phenomes was observed, it was largely driven by differences in growth across treatments. DTV increased growth, suggesting that it represents a promising coral restoration tool to improve growth in nursery settings [as in (45)]. However, experimental exposure to DTV did not facilitate the maintenance of Fv/Fm during subsequent thermal challenge. It is possible that the DTV treatment used here was insufficient to prime corals [reviewed in (46)]. Unique DTV temperature regimes and timing of exposure have previously resulted in variable phenotypic outcomes for the corals *Montipora capitata* (21) and *Acropora aspera* (47). In *M. capitata*, only two of four variability pre-exposure profiles altered gene expression and resulted in improved thermal tolerance in stress tests 4 months later (21). In addition, in *A. aspera*, exposure to DTV in the month preceding a heat challenge had a

larger, and ultimately deleterious, effect on heat tolerance compared to corals that experienced 1.5 years of preconditioning to variable temperatures (47). Previous work has also demonstrated that DTV can have negative effects when additional heat stress is present [e.g., (48)], and the BTRC reached $\sim 7^\circ$ heating weeks in the year prior to coral collection (2015; NOAA Coral Reef Watch v3.1), which could have influenced responses to DTV.

Elevated growth of L1 compared to L2 was evident not only during the mesocosm DTV experiment but also in coral cores from across the BTRC belonging to the same cryptic lineages. Century-scale data from cores of long-lived corals such as *S. siderea* allow investigation into the impact of long-term environmental conditions on coral growth and, ultimately, health. Here, cores sampled across inshore and offshore environments of the BTRC show that L1 maintained greater linear extension, lower skeletal density, and trended toward greater overall calcification compared to L2. Previous coring studies on *S. siderea* demonstrate that reef environments play an important role in shaping long-term growth trajectories. Specifically, in *S. siderea* sampled from the southern Mesoamerican Barrier Reef System, fore-reef corals exhibited long-term declines in skeletal extension rates whereas nearshore and back-reef coral extension rates were stable (49, 50). The authors propose that resilience of nearshore and back-reef corals is linked to their exposure to greater diurnal and seasonal thermal variability (50). In contrast, more widespread sampling of *S. siderea* cores across the entire Mesoamerican Barrier Reef System revealed declines in skeletal extension rates only for nearshore corals, which was attributed to exposure to land-based anthropogenic stressors and ocean warming (51). Although it is possible that the lineage differences in historical growth found here are driven by reef environments, because lineage and environment were almost fully confounded in this coring sampling design, it is also possible that previous works on coral growth trajectories are complicated by the presence of *S. siderea* cryptic diversity across the Mesoamerican Barrier Reef System. Future work sampling cores from coexisting lineages would disentangle the role of environmental and genetic factors in determining long-term growth trajectories. A more thorough characterization of general environmental conditions at these sites (e.g., nutrient concentrations, pH, and dissolved oxygen) is also needed as sites where L1 and L2 are sympatric suggest other environmental characteristics could be driving differentiation and distributions of *S. siderea* cryptic lineages.

S. siderea is a horizontally transmitting, gonochoric broadcast spawning coral, with colonies of separate sexes spawning gametes to produce aposymbiotic larvae that spend time in the water column before settling, leading to the potential for broad population connectivity across great distances [up to 1200 km; (52)]. Although much more work is warranted, we propose that, in the BTRC, the distinct light environments across inshore and offshore reefs along with physical characteristics of the archipelago (39, 53) result in spatially varying selection on cryptic lineages that are uniquely adapted to distinct light environments. Although few sites were found to host multiple lineages and no site hosted all three, sampling for this study was limited to < 8 m and exact depths of corals were not recorded. Therefore, we hypothesize that additional sampling across depth within individual sites will reveal differential depth distributions of the lineages that reflect patterns observed across inshore and offshore environments (i.e., L1 associated with higher light and L2 associated with lower light). As was previously demonstrated by Quigley *et al.* (54), it is also likely that environmental pools of algae

are much more diverse than communities hosted by adult corals, and therefore once recruits begin establishing symbiosis, algal symbionts likely compete through a “winnowing” process with dominance depending on local environmental conditions (i.e., light and depth) that are further shaped by coral colony and skeleton morphology (28). Surviving recruits of distinct lineages then develop associations with specific Symbiodiniaceae in environments that differ in temperature, light, and nutrients, likely resulting in further acclimation to local conditions. Together, these genetic and environmental factors interact to determine the patterns of responses observed here, where unique holobiont partners shape variation in phenomes, response to thermal challenge, and historical growth. Ultimately, reciprocal transplant experiments are needed to disentangle the relative roles of adaptation and acclimation in the observed phenotypes between lineages. In addition, whole-genome sequencing of the cryptic lineages in this system represents an important future goal, which will help uncover their evolutionary history and potentially identify the genomic basis of their distinct holobiont phenomes. This work highlights the importance of understanding cryptic coral diversity when determining species responses to future climate change and in restoration planning.

MATERIALS AND METHODS

Identification of cryptic lineages

In August 2016, nine visually healthy colonies (20 to 30 cm in diameter) of the reef-building coral species *S. siderea* were collected between 2.5 and 8 m in depth at each of six sites (54 colonies total, permit SE/A-36-16). Sites included three inshore (PD, SP, and CI) and three offshore (BN, BS, and CA) sites in the BTRC, Panamá. Colonies were maintained in flow-through seawater at the Smithsonian Tropical Research Institute in the BTRC prior to being shipped to the University of North Carolina at Chapel Hill overnight.

Upon return, small tissue samples (~ 1 cm²) were collected from each colony and holobiont DNA was extracted ($N = 54$) using a modified phenol-chloroform method as in (55). DNA extracts were cleaned using Zymo Genomic DNA Clean and Concentrator kits, and concentrations were assessed using a Quant-iT PicoGreen dsDNA assay kit (Thermo Fisher Scientific). Samples of sufficient concentration (51/54 putative genotypes) were prepared for 2b-RADseq (56), with 10 technical replicates to enable clone identification. A total of 61 samples were successfully sequenced across one lane of Illumina HiSeq 2500 using single-end 50–base pair (bp) sequencing at the Tufts University Core Facility (TUCF).

2b-RADseq analysis followed the pipeline presented at https://github.com/z0on/2bRAD_denovo (accessed August 2021). Raw reads were trimmed and demultiplexed, and cutadapt (57) removed reads with Phred quality score less than 15 and reads < 36 bp in length. Because no *S. siderea* genome is available, a de novo reference was created. Following Rippe *et al.* (34), Symbiodiniaceae contamination was removed by mapping reads to concatenated genomes from four Symbiodiniaceae genera: *Symbiodinium* (58), *Breviolum* (59), *Cladocopium* (60), and *Durusdinium* (61) using Bowtie2 v2.4.2 (62). Putative symbiont contamination was removed and CD-HIT v4.7 (63) clustered and assembled remaining reads into a de novo reference consisting of 30 pseudochromosomes. Reads were mapped to this de novo reference using Bowtie2 v2.4.2 with default parameters, and ANGSD v0.935 (64) was used for genotyping (using likelihood estimates) and identifying single-nucleotide polymorphisms

(SNPs). Standard filters were used to retain loci, which included $\geq 2x$ coverage, loci present in at least 80% of individuals, a minimum mapping quality score of 20, a minimum quality score of 25, a strand bias P value of $>1 \times 10^{-5}$, a heterozygosity bias of $>1 \times 10^{-5}$, an SNP P value of 1×10^{-5} , and a minimum minor allele frequency of >0.05 , excluded all triallelic sites, and removed reads with multiple best hits. To distinguish putative clones, a hierarchical clustering tree (*hclust*) was constructed based on pairwise IBS values across all samples. Clones were determined using the similarity of technical replicates as a cutoff, and only one pair of clones was detected at PD (I4G and I4F; fig. S1C). The clone pair with the lower total read count (I4G) was removed from all further analyses.

Population structure on the dataset with the clone removed (8105 SNPs) was determined using three methods: (i) hierarchical clustering of pairwise IBS values, (ii) PCoA based on the IBS matrix, and (iii) admixture proportions of individuals across sites. A height of 0.265 was used as the cutoff from the clustering dendrogram to distinguish three lineages (fig. S1D). PCoA was performed on the covariance matrix in R v4.0.2 (65) using *capscale* [with null model, package = *vegan*; (66)] and was used in combination with the hierarchical clustering results to determine an optimal K of 3. NgsAdmix v1.3.0 (67) with $K = 3$ then determined the proportion of each individual's ancestry that corresponded to each lineage [lineage 1 (L1), lineage 2 (L2), and lineage 3 (L3)]. NgsRelate (68) was used to assess pairwise relatedness (*rab*) among individuals within each lineage.

To estimate genetic differentiation, a different set of filters were used to retain loci, which included loci present in at least 80% of individuals, a minimum mapping quality score of 25, a minimum quality score of 30, a strand bias P value of $>1 \times 10^{-5}$, and a heterozygosity bias of $>1 \times 10^{-5}$, excluded all triallelic sites, removed reads with multiple best hits, and passed the lumped paralog filter (770,398 SNPs). Genetic differentiation between lineages was estimated using ANGSD to find site allele frequency (SAF) for each lineage, after which realSFS determined the site frequency spectrum (SFS) for all lineage pairwise comparisons. Calculated SAFs and SFSs were then used to calculate global F_{ST} , reported as weighted global F_{ST} values. Pearson's chi-square test was used to determine whether the distribution of L1 and L2 was dependent on reef type (inshore or off-shore), excluding L3 individuals. All statistical analyses and data visualizations presented here were performed using R v4.0.2 (65).

Characterizing baseline bacterial and Symbiodiniaceae communities

To characterize bacterial and Symbiodiniaceae communities associated with these *S. siderea* lineages, metabarcoding libraries were generated using a series of polymerase chain reaction amplifications for the V4/V5 region of the bacterial 16S ribosomal RNA (rRNA) gene (69, 70) and the ITS2 region of Symbiodiniaceae ribosomal DNA (71, 72), respectively. These libraries included both the colonies described above (but with L3 excluded; baseline time point) as well as fragments of these same colonies after a 50-day DTV experiment (post-DTV time point; described in detail below). Samples were sequenced (paired-end 250 bp) on an Illumina MiSeq at the TUCF and both time points were analyzed together. For additional details on library preparation, refer to the Supplementary Materials.

16S sequencing data were analyzed using DADA2 (73), which conducted quality filtering and identified 17,903 ASVs in 131 successfully sequenced samples (L3 individuals excluded). ASVs matching mitochondrial, chloroplast, and nonbacterial sequences

were removed (1487 ASVs) followed by an additional 160 ASVs identified in negative controls by the package *decontam*, leaving 16,256 ASVs and 131 samples with complete metadata remaining ($N = 47$ baseline samples and $N = 84$ post-DTV samples). Taxonomy was assigned using the Silva v132 database (74) and by using blast+ against the National Center for Biotechnology Information (NCBI) nucleotide database (75). ASVs were checked for eukaryotic contamination, but none was detected. Counts were rarefied to 1000 reads per sample using the package *vegan*, leaving 6144 ASVs and 47 samples for the baseline time point and 5799 ASVs and 69 samples for the post-DTV time point. ASV richness and evenness in addition to Shannon and Simpson's diversity indices were calculated from cleaned data (contaminant ASVs removed but nonrarefied) using the *estimate_richness* function [package = *phyloseq*; (76)]. An analysis of variance (ANOVA) tested for differences in diversity metrics across fixed effects of host lineage for baseline and host lineage plus DTV treatment for post-DTV. Bray-Curtis dissimilarity PCoAs were conducted on all ASVs (relative abundance of rarefied datasets) using *phyloseq* for samples with complete lineage and DTV treatment metadata. *Vegan* and *pairwise.adonis* were implemented for statistical analyses of bacterial community differences and dispersion. 16S analyses were conducted on both rarefied and nonrarefied data, which resulted in similar patterns.

ITS2 data were submitted to SymPortal (32) to identify ITS2 type profiles. Successfully sequenced samples with corresponding metadata and excluding L3 individuals ($N = 47$ baseline samples and $N = 84$ post-DTV samples) were visualized for differences between host lineages for baseline samples and host lineages and DTV treatment for post-DTV samples. DIVs were summed by majority ITS2 sequence before calculating relative abundances. Relative abundances of majority ITS2 sequences were compared with bar plots using *phyloseq*, and a Kruskal-Wallis test (*kruskal.test*) tested for differences in the proportion of D1 majority ITS2 sequences across L1 and L2.

Assessing baseline holobiont phenomes and skeleton morphologies

Coral colonies were sectioned into fragments using a tile saw (RIDGID) and affixed to pre-labeled plastic petri dishes using cyanoacrylate glue (IC-Gel Insta Cure; BSI). All fragments were maintained in aquaria for 16 days at 28°C with standardized light conditions of 400 $\mu\text{mol photon m}^{-2} \text{s}^{-1}$ on a 12-hour:12-hour light:dark cycle using full-spectrum light-emitting diodes (Euphotica; 120 W, 20,000K) based on Rodas *et al.* (77). After this recovery period, baseline phenomic metrics of coral host and algal symbiont health were assessed by flash freezing one fragment of each genotype. Flash-frozen fragments were thawed, and tissue was removed via airbrush and seawater, homogenized, and centrifuged to separate host and symbiont fractions, which were divided into four aliquots. One symbiont aliquot was used for symbiont cell counts, and all other host and symbiont aliquots were disrupted using a bead mill homogenizer (Omni Bead Mill 24; GA, USA) with a high-throughput hub at 6 m s^{-1} for 2 min for downstream phenomic assessments.

Total host protein was quantified using the Bradford method (78) with absorbances read at 595 nm on a microplate reader (Biotek Synergy H1; CA, USA). Data were converted from absorbance to total protein concentrations ($\mu\text{g } \mu\text{l}^{-1}$) using a standard curve of bovine serum albumin and then normalized to surface area. Total host and algal symbiont carbohydrates were quantified using the phenol-sulfuric

acid method (79) with absorbances read at 500 nm. Carbohydrate values (mg ml^{-1}) were calculated from raw absorbance using a D-glucose standard curve and then normalized to surface area. This method measures all monosaccharides, which includes glucose, the main by-product of photosynthesis that is translocated from algal symbiont to coral (80). Algal cell density was quantified in triplicate using the hemocytometer method (81) and then normalized to surface area. Symbiont photosynthetic pigments [chlorophyll a (Chl a)] were measured spectrophotometrically, read at 663 and 630 nm, calculated following Eq. 1 below (82) where A_{663} represents blank-corrected absorbance values at 663 nm and A_{630} represents blank-corrected absorbance values at 630 nm, and then normalized to surface area

$$\text{Chl a } (\mu\text{g ml}^{-1}) = 13.31 \times A_{663} - 0.27 \times A_{630} \quad (1)$$

Tissue thickness (mm) for all fragments was measured with calipers after tissue was removed, and corallite surface area (mm^2) was measured following previously established methods (83). Briefly, the polygon tool in ImageJ (84) measured the area of seven corallites from each fragment in pixels, which was converted to mm^2 using a size standard in each photograph.

Skeletons from the baseline time point were scanned at high resolution (>1200 dpi; Epson Perfection V550), and additional skeleton morphometrics were quantified using ImageJ (84). Measurements were taken randomly from 5 to 10 corallites per fragment that were perpendicular to the field of view and not in a budding state nor at the colony margins to avoid areas of recent growth. Several skeletal morphometric traits were measured, including calyx diameter, septal length and width from the primary cycle, intercorallite (i.e., theca) wall thickness, corallite spacing, and corallite density (# corallites cm^{-2}).

LEF, which describes the optical property of the skeleton to collect and enhance the light field, was estimated by quantifying relative changes in the intensification of local illumination on a naked coral skeleton due to multiple light scattering (85). Before measuring the LEF, coral skeletons were soaked in 10% commercial bleach for 48 hours and dried at 50° to 60°C for 48 hours to avoid absorption from the remaining organic matter. Detailed descriptions of the method can be found in (28), but briefly, the LEF was measured in triplicate for each fragment and expressed as the ratio of reflected light from a skeleton illuminated by a light source and the reflected light from a reference (black fabric). Illumination was provided by a linearly polarized continuous wave laser diode (532 nm) coupled with a lens to a miniature isotropic probe fabricated with standard-fused silica step-index optical fibers (numerical aperture = 0.22, 200 μm in diameter core). This probe was used as a light source and placed in proximity to the cavities of the skeleton. The light scattered by the skeleton was measured using a miniature spectroradiometer (Ocean Optics Inc.). Although the LEF reflects the maximum potential ability of the coral skeleton to enhance the light field for algal photosynthesis in the coral tissue (86), it is not a descriptor of coral tissue pigmentation.

To characterize baseline holobiont phenomic differences across lineages, all host and symbiont physiology metrics were log transformed and combined in PCAs using the *FactoMineR* package. Significance of the fixed effect of lineage was assessed with PERMANOVA, using the *adonis* function (package = *vegan*). Effect size was determined using partial ω^2 values calculated with the *adonis_OmegaSq* function (package = *MicEco*). The same method and PERMANOVA model that were used to assess baseline phenome PCAs was also used

for the skeleton morphology PCA. A separate linear model was used to assess the main effect of lineage on LEF. For all linear models presented here, assumptions and model fit were assessed visually using the *check_model* function (package = *performance*) and pairwise comparisons were calculated using *emmeans*.

Testing responses to thermal variability and thermal challenge across lineages

To determine how host lineages respond to thermal variability and thermal challenge, we exposed fragments of each colony to a 50-day DTV experiment, followed by thermal challenge and recovery. In situ temperature data were continuously collected every 15 min for ~ 1 year prior to colony collection, with HOBO ProV2 temperature loggers (Onset, Bourne, MA) deployed between 1 and 4 m in depth at each of the six sites (Fig. 1B) from 10 June 2015 to 14 August 2016. Loggers were recovered from four sites, including three inshore (CI, PD, and SP) and one offshore (CA). Differences in daily mean temperature and daily temperature range (reported in table S1A) across sites were determined using a one-way ANOVA with Tukey's post hoc tests (Fig. 1B and table S2). Two DTV treatments were designed based on these in situ temperature data. The control treatment (no DTV) was maintained at 29.5°C , representing the overall daily mean of all sites ($29.6^\circ \pm 0.02^\circ\text{C}$; table S1). The DTV treatment had a minimum temperature of 28.5°C with daily increases of 3°C (28.5° to 31.5°C), and this treatment was informed by the highest in situ DTV observed (3.2°C at CI) (table S1).

Colony fragments ($N = 18$ genotypes per tank, three aquaria per treatment) were randomly distributed into treatment aquaria for 16 days at 28°C (recovery), followed by 15 days of acclimation to experimental conditions. Next, a 50-day DTV experiment was conducted followed by a 15-day thermal challenge (32°C) and 16-day recovery period (fig. S2). Differences in daily temperature parameters (variability, mean, maximum, and minimum) across treatments during the 50-day DTV treatment were determined using a one-way ANOVA, and the effect size (i.e., variance in temperature parameter explained by experimental treatment) was determined using eta-square (η^2) values calculated using the *eta_squared* function (package = *effectsize*). Distinct treatments were maintained over the course of the 50-day DTV treatment (fig. S11 and table S14). Throughout the experiment, light conditions were maintained at $400 \mu\text{mol photon m}^{-2} \text{ s}^{-1}$ on a 12-hour:12-hour light:dark cycle. Corals were fed freshly hatched *Artemia* sp. nauplii two to three times weekly, at night, and were allowed to feed for 1 hour before resuming recirculating flow in the aquaria. For more detailed experimental information, including water quality, see the Supplementary Materials.

Coral growth was estimated using the buoyant weight method under standard conditions (28°C and 33 parts per thousand salinity) with a bottom-loading balance (precision = 0.0001 g; Mettler-Toledo) at four time points: after acclimation (T_0), during DTV (T_1), at the end of DTV (T_2), and at the end of recovery (T_3) (see experimental timeline in fig. S2). Growth was calculated as a specific growth rate per day through DTV treatment (T_0 to T_2) as well as through heat stress and recovery (T_2 to T_3). Immediately after buoyant weighing, corals were imaged to quantify surface area for physiology standardization with a CoralWatch Health Chart (87). Distance between the camera and corals as well as lighting were standardized. Surface area measurements were obtained using ImageJ (84), and only live tissue was included in surface area normalizations. The effect of DTV and host lineage on growth was assessed separately for two durations: (i)

throughout the 50-day DTV treatment and (ii) during the thermal challenge and recovery periods. For both durations, linear mixed models (package = *lme4*) were implemented with main effects of treatment and lineage and a random effect of genotype.

Photochemical efficiency of photosystem II (Fv/Fm) was measured in triplicate for each fragment using a Diving PAM (Walz) at seven time points: once at the end of DTV, three times during thermal challenge, and three times during recovery. For all time points, corals were dark acclimated for at least 30 min before measurements, which started between 17:00 and 19:00 and ended between 20:00 and 22:00. Measurements were made using a saturation pulse width of 0.6 s at full-strength light intensity, electronic signal damping of 2, and gain of 4. A linear mixed model was implemented to assess the interactive effects of time, lineage, and DTV treatment (with a random effect of coral genotype) on Fv/Fm throughout the thermal challenge and recovery periods.

Phenomic metrics of holobiont health were assessed by flash freezing fragments following final recovery and following the same methods used for baseline holobiont phenomes described above. To characterize phenome-wide responses, all metrics were log transformed and combined in PCAs using the *FactoMineR* package. Significance of each factor (fixed effects of DTV treatment and host lineage) were assessed with PERMANOVAs, and the effect size of each factor was determined using ω^2 values calculated as described above. For all end of experiment models (i.e., when more than one factor of interest was present), models were selected based on a backward selection method, where only significant interaction terms were maintained in the model.

Coral holobiont DNA was also subsampled, preserved in 100% ethanol, and stored at -80°C at the end of the 50-day DTV treatment to assess changes in bacterial and Symbiodiniaceae communities in response to DTV, following methods described above (figs. S6 and S7, respectively).

Historical growth estimates via sclerochronology

In 2015, a total of 39 cores of large *S. siderea* (~1 m in diameter) colonies were collected from four pairs of inshore-offshore reef sites in the BTRC (permit SE/A-28-15) using a hydraulic core drill following methods previously described in detail (51, 88). The eight sites where cores were collected include the six sites detailed above (Fig 1A; PD, SP, CI, BN, BS, and CA), as well as two additional sites (inshore: PL; offshore: DM). From each site, five healthy colonies were randomly selected for coring. In some cases, less than five colonies were sampled due to a lack of corals of sufficient size. Skeletal cores were preserved in 200-proof ethanol and transported to the UNC-Chapel Hill, where they were scanned using x-ray computed tomography to visualize annual density growth bands [following (51, 88)]. In brief, boundaries between semiannual density bands were manually delineated, and linear transects were traced down the central axis of three corallites to estimate growth (fig. S10B). Following a previously established protocol (89), nine density standards were included in each scan to facilitate converting skeletal density measurements from CT Hounsfield units to g cm^{-3} . Linear extension was measured in the image viewing software Horos v2.0.2 as the width of each annual density band couplet, and calcification (g cm^{-2}) was calculated as the product of skeletal density and linear extension.

In 2023, tissue was scraped from the surface of remaining *S. siderea* cores ($N = 38$), and DNA was isolated using Qiagen Blood and Tissue

kits following the manufacturer's instructions. DNA extracts were cleaned and prepared for 2b-RADseq following methods detailed above. Samples were sequenced at the TUCF along with replicate samples from the original lineage dataset to facilitate identifying the lineage of each core. After lineage assignment, $N = 24$ cores remained with both growth chronology and lineage assignment. A linear model with fixed effect of lineage was used to test for lineage differences in skeletal density, linear extension, and calcification separately for two separate time intervals: (i) all data (1880 to 2014) and (ii) recent data (1980 to 2014). Analyses were separated into these two time intervals to confirm that lineage-specific historical growth patterns were consistent regardless of the number of data points per core (i.e., core age) as sample size decreases moving back in time. The linear model results were consistent regardless of time interval; therefore, results from analyses of recent data are presented in the main text, and results from all data are found in the Supplementary Materials.

Monthly historic sea surface temperature (SST) data were obtained from 1870 to 2023 from the Hadley Centre Sea Ice and Sea Surface Temperature (HadISST) dataset (90) for the 1° latitude-longitude grid that covers all sampling sites. The HadISST database combines in situ and satellite observations of global SST data, making it an ideal resource for assessing historic trends in temperature [e.g., (91, 92)]. Monthly temperature observations were averaged to estimate annual mean (January to December) and annual summer mean (August to November) for the region. Linear models with fixed effects of temperature (either annual summer mean or annual mean) and lineage were used to explore whether historical calcification was modulated by temperature changes and whether these changes were different between lineages. These linear models were completed with data from the two time intervals of historical growth data (i.e., all data and recent data). In addition, a separate linear model was used to assess whether annual mean and annual summer mean increased between 1870 and 2023 in the BTRC.

Supplementary Materials

This PDF file includes:

Supplementary Results
Supplementary Materials and Methods
Figs. S1 to S11
Tables S1 to S14

REFERENCES AND NOTES

- H. Pörtner, D. Roberts, V. Masson-Delmotte, P. Zhai, M. Tignor, E. Poloczanska, K. Mintenbeck, A. Alegria, M. Nicolai, A. Okem, J. Petzold, B. Rama, IPCC Special Report on the Ocean and Cryosphere in a Changing Climate (IPCC, 2019); <https://ipcc.ch/srocc/>.
- G. N. Somero, The physiology of climate change: How potentials for acclimatization and genetic adaptation will determine 'winners' and 'losers'. *J. Exp. Biol.* **213**, 912–920 (2010).
- L.-M. Chevin, R. Lande, G. M. Mace, Adaptation, plasticity, and extinction in a changing environment: Towards a predictive theory. *PLoS Biol.* **8**, e1000357 (2010).
- R. Costanza, R. de Groot, P. Sutton, S. van der Ploeg, S. J. Anderson, I. Kubiszewski, S. Farber, R. K. Turner, Changes in the global value of ecosystem services. *Glob. Environ. Chang.* **26**, 152–158 (2014).
- M. Spalding, L. Burke, S. A. Wood, J. Ashpole, J. Hutchison, P. z. Ermgassen, Mapping the global value and distribution of coral reef tourism. *Mar. Policy* **82**, 104–113 (2017).
- F. M. França, C. E. Benkwitt, G. Peralta, J. P. W. Robinson, N. A. J. Graham, J. M. Tylianakis, E. Berenguer, A. C. Lees, J. Ferreira, J. Louzada, J. Barlow, Climatic and local stressor interactions threaten tropical forests and coral reefs. *Philos. Trans. R. Soc. London Ser. B Biol. Sci.* **375**, 20190116 (2020).
- B. E. Brown, Coral bleaching: Causes and consequences. *Coral Reefs* **16**, S129–S138 (1997).
- C. Mellin, S. Brown, N. Cantin, E. Klein-Salas, D. Mouillot, S. F. Heron, D. A. Fordham, Cumulative risk of future bleaching for the world's coral reefs. *Sci. Adv.* **10**, eadn9660 (2024).

9. A. G. Grottoli, M. E. Warner, S. J. Levas, M. D. Aschaffenburg, V. Schoepf, M. McGinley, J. Baumann, Y. Matsui, The cumulative impact of annual coral bleaching can turn some coral species winners into losers. *Glob. Chang. Biol.* **20**, 3823–3833 (2014).
10. C. B. Bove, M. V. Ingersoll, S. W. Davies, Help me, symbionts, you're my only hope: Approaches to accelerate our understanding of coral holobiont interactions. *Integr. Comp. Biol.* **62**, 1756–1769 (2022).
11. Z. L. Fuller, V. J. L. Mocellin, L. A. Morris, N. Cantin, J. Shepherd, L. Sarre, J. Peng, Y. Liao, J. Pickrell, P. Andolfatto, M. Matz, L. K. Bay, M. Przeworski, Population genetics of the coral *Acropora millepora*: Toward genomic prediction of bleaching. *Science* **369**, eaba4674 (2020).
12. D. P. Manzello, M. V. Matz, I. C. Enochs, L. Valentino, R. D. Carlton, G. Kolodziej, X. Serrano, E. K. Towle, M. Jankulak, Role of host genetics and heat-tolerant algal symbionts in sustaining populations of the endangered coral *Orbicella faveolata* in the Florida Keys with ocean warming. *Glob. Chang. Biol.* **25**, 1016–1031 (2019).
13. M. Ziegler, F. O. Seneca, L. K. Yum, S. R. Palumbi, C. R. Voolstra, Bacterial community dynamics are linked to patterns of coral heat tolerance. *Nat. Commun.* **8**, 14213 (2017).
14. D. Bickford, D. J. Lohman, N. S. Sodhi, P. K. L. Ng, R. Meier, K. Winker, K. K. Ingram, I. Das, Cryptic species as a window on diversity and conservation. *Trends Ecol. Evol.* **2007**, 148–155 (2007).
15. C. G. B. Grupstra, M. Gómez-Corralles, J. E. Fifer, H. E. Aichelman, K. S. Meyer-Kaiser, C. Prada, S. W. Davies, Integrating cryptic diversity into coral evolution, symbiosis and conservation. *Nat. Ecol. Evol.* **8**, 622–636 (2024).
16. N. H. Rose, R. A. Bay, M. K. Morikawa, L. Thomas, E. A. Sheets, S. R. Palumbi, Genomic analysis of distinct bleaching tolerances among cryptic coral species. *Proc. R. Soc. London Ser. B Biol. Sci.* **288**, 20210678 (2021).
17. P. W. Boyd, C. E. Cornwall, A. Davison, S. C. Doney, M. Fourquez, C. L. Hurd, I. D. Lima, A. McMinn, Biological responses to environmental heterogeneity under future ocean conditions. *Glob. Chang. Biol.* **22**, 2633–2650 (2016).
18. T. A. Oliver, S. R. Palumbi, Do fluctuating temperature environments elevate coral thermal tolerance? *Coral Reefs* **30**, 429–440 (2011).
19. A. Safaie, N. J. Silbiger, T. R. McClanahan, G. Pawlak, D. J. Barshis, J. L. Hench, J. S. Rogers, G. J. Williams, K. A. Davis, High frequency temperature variability reduces the risk of coral bleaching. *Nat. Commun.* **9**, 1671 (2018).
20. M. D. Massey, M. K. Fredericks, D. Malloy, S. Arif, J. A. Hutchings, Differential reproductive plasticity under thermal variability in a freshwater fish (*Danio rerio*). *Proc. R. Soc. London Ser. B Biol. Sci.* **289**, 20220751 (2022).
21. C. Drury, J. Dilworth, E. Majerová, C. Caruso, J. B. Greer, Expression plasticity regulates intraspecific variation in the acclimatization potential of a reef-building coral. *Nat. Commun.* **13**, 4790 (2022).
22. E. B. Rivest, S. Comeau, C. E. Cornwall, The role of natural variability in shaping the response of coral reef organisms to climate change. *Curr. Clim. Chang. Rep.* **3**, 271–281 (2017).
23. V. Schoepf, M. U. Jung, M. T. McCulloch, N. E. White, M. Stat, L. Thomas, Thermally variable, macrotidal reef habitats promote rapid recovery from mass coral bleaching. *Front. Mar. Sci.* **7**, 245 (2020).
24. P. J. Edmunds, Effect of acclimatization to low temperature and reduced light on the response of reef corals to elevated temperature. *Mar. Biol.* **156**, 1797–1808 (2009).
25. J. Fifer, B. Bentlage, S. Lemer, A. G. Fujimura, M. Sweet, L. J. Raymundo, Going with the flow: How corals in high-flow environments can beat the heat. *Mol. Ecol.* **30**, 2009–2024 (2021).
26. C. Prada, M. E. Hellberg, Speciation-by-depth on coral reefs: Sympatric divergence with gene flow or cryptic transient isolation? *J. Evol. Biol.* **34**, 128–137 (2021).
27. P. Bongaerts, I. R. Cooke, H. Ying, D. Wels, S. den Haan, A. Hernandez-Agreda, C. A. Brunner, S. Dove, N. Englebert, G. Eyal, S. Forêt, M. Grinblat, K. B. Hay, S. Harii, D. C. Hayward, Y. Lin, M. Mihaljević, A. Moya, P. Muir, F. Sinniger, P. Smallhorn-West, G. Torda, M. A. Ragan, M. J. H. van Oppen, O. Hoegh-Guldberg, Morphological stasis masks ecologically divergent coral species on tropical reefs. *Curr. Biol.* **31**, 2286–2298 (2021).
28. S. Enriquez, E. R. Méndez, O. Hoegh-Guldberg, R. Iglesias-Prieto, Key functional role of the optical properties of coral skeletons in coral ecology and evolution. *Proc. R. Soc. London Ser. B Biol. Sci.* **284**, 20161667 (2017).
29. A. M. A. Matias, I. Popovic, J. A. Thia, I. R. Cooke, G. Torda, V. Lukoschek, L. K. Bay, S. W. Kim, C. Riginos, Cryptic diversity and spatial genetic variation in the coral *Acropora tenuis* and its endosymbionts across the great barrier reef. *Evol. Appl.* **16**, 293–310 (2023).
30. C. D. Kenkel, E. Meyer, M. V. Matz, Gene expression under chronic heat stress in populations of the mustard hill coral (*Porites astreoides*) from different thermal environments. *Mol. Ecol.* **22**, 4322–4334 (2013).
31. S. Barfield, S. W. Davies, M. V. Matz, Evidence of sweepstakes reproductive success in a broadcast-spawning coral and its implications for coral metapopulation persistence. *Mol. Ecol.* **32**, 696–702 (2023).
32. B. C. Hume, E. G. Smith, M. Ziegler, H. J. M. Warrington, J. A. Burt, T. C. Lajeunesse, J. Wiedenmann, C. R. Voolstra, SymPortal: A novel analytical framework and platform for coral algal symbiont next-generation sequencing *ITS2* profiling. *Mol. Ecol. Resour.* **19**, 1063–1080 (2019).
33. J. E. Fifer, N. Yasuda, T. Yamakita, C. B. Bove, S. W. Davies, Genetic divergence and range expansion in a western North Pacific coral. *Sci. Total Environ.* **813**, 152423 (2022).
34. J. P. Rippe, G. B. Dixon, Z. L. Fuller, Y. Liao, M. Matz, Environmental specialization and cryptic genetic divergence in two massive coral species from the Florida Keys Reef Tract. *Mol. Ecol.* **30**, 3468–3484 (2021).
35. R. J. Eckert, M. S. Studivan, J. D. Voss, Populations of the coral species *Montastraea cavernosa* on the Belize Barrier Reef lack vertical connectivity. *Sci. Rep.* **9**, 7200 (2019).
36. S. Starko, J. E. Fifer, D. C. Claar, S. W. Davies, R. Cuning, A. C. Baker, J. K. Baum, Marine heatwaves threaten cryptic coral diversity and erode associations among coevolving partners. *Sci. Adv.* **9**, eadf0954 (2023).
37. N. H. Rose, R. A. Bay, M. K. Morikawa, S. R. Palumbi, Polygenic evolution drives species divergence and climate adaptation in corals. *Evolution* **72**, 82–94 (2018).
38. A. E. Adelson, A. H. Altieri, X. Boza, R. Collin, K. A. Davis, A. Gaul, S. N. Giddings, V. Reed, G. Pawlak, Seasonal hypoxia and temperature inversions in a tropical bay. *Limnol. Oceanogr.* **67**, 2174–2189 (2022).
39. J. K. Briand, H. M. Guzmán, J. M. Sunday, Spatio-temporal patterns in coral reef composition and function across an altered environmental gradient: A 15-year study in the Caribbean. *Front. Mar. Sci.* **9**, 977551 (2023).
40. T. Scheufen, R. Iglesias-Prieto, S. Enriquez, Changes in the number of symbionts and *Symbiodinium* cell pigmentation modulate differentially coral light absorption and photosynthetic performance. *Front. Mar. Sci.* **4**, 309 (2017).
41. R. M. Vásquez-Elizondo, L. Legaria-Moreno, M. Á. Pérez-Castro, W. E. Krämer, T. Scheufen, R. Iglesias-Prieto, S. Enriquez, Absorbance determinations on multicellular tissues. *Photosynth. Res.* **132**, 311–324 (2017).
42. R. N. Silverstein, R. Cuning, A. C. Baker, Change in algal symbiont communities after bleaching, not prior heat exposure, increases heat tolerance of reef corals. *Glob. Chang. Biol.* **21**, 236–249 (2015).
43. F. J. Pollock, R. McMinds, S. Smith, D. G. Bourne, B. L. Willis, M. Medina, R. V. Thurber, J. R. Zaneveld, Coral-associated bacteria demonstrate phylosymbiosis and copylogeny. *Nat. Commun.* **9**, 4921 (2018).
44. J. E. Fifer, V. Bui, J. T. Berg, N. Kriefall, C. Klepac, B. Bentlage, S. W. Davies, Microbiome structuring within a coral colony and along a sedimentation gradient. *Front. Mar. Sci.* **8**, 805202 (2022).
45. A. DeMerlis, A. Kirkland, M. L. Kaufman, A. B. Mayfield, N. Formel, G. Kolodziej, D. P. Manzello, D. Lirman, N. Traylor-Knowles, I. C. Enochs, Pre-exposure to a variable temperature treatment improves the response of *Acropora cervicornis* to acute thermal stress. *Coral Reefs* **41**, 435–445 (2022).
46. S. Hackerott, H. A. Martell, J. M. Eirin-Lopez, Coral environmental memory: Causes, mechanisms, and consequences for future reefs. *Trends Ecol. Evol.* **36**, 1011–1023 (2021).
47. V. Schoepf, H. Sanderson, E. Larcombe, Coral heat tolerance under variable temperatures: Effects of different variability regimes and past environmental history vs. current exposure. *Limnol. Oceanogr.* **67**, 404–418 (2022).
48. C. N. Klepac, D. J. Barshis, Reduced thermal tolerance of massive coral species in a highly variable environment. *Proc. R. Soc. London Ser. B Biol. Sci.* **287**, 20201379 (2020).
49. K. D. Castillo, J. B. Ries, J. M. Weiss, Declining coral skeletal extension for forereef colonies of *Siderastrea siderea* on the mesoamerican barrier reef system, Southern Belize. *PLOS ONE* **6**, e14615 (2011).
50. K. D. Castillo, J. B. Ries, J. M. Weiss, F. P. Lima, Decline of forereef corals in response to recent warming linked to history of thermal exposure. *Nat. Clim. Chang.* **2**, 756–760 (2012).
51. J. H. Baumann, J. B. Ries, J. P. Rippe, T. A. Courtney, H. E. Aichelman, I. Westfield, K. D. Castillo, Nearshore coral growth declining on the Mesoamerican Barrier Reef System. *Glob. Chang. Biol.* **25**, 3932–3945 (2019).
52. F. L. D. Nunes, R. D. Norris, N. Knowlton, Long distance dispersal and connectivity in amphiatlantic corals at regional and basin scales. *PLOS ONE* **6**, e22298 (2011).
53. H. M. Guzmán, P. A. G. Barnes, C. E. Lovelock, I. C. Feller, A site description of the CARICOMP mangrove, seagrass and coral reef sites in Bocas Del Toro, Panamá. *Caribb. J. Sci.* 430–440 (2005).
54. K. M. Quigley, L. K. Bay, B. L. Willis, Temperature and water quality-related patterns in sediment-associated *Symbiodinium* communities impact symbiont uptake and fitness of juveniles in the genus *Acropora*. *Front. Mar. Sci.* **4**, 401 (2017).
55. S. W. Davies, M. Rahman, E. Meyer, E. A. Green, E. Buschiazio, M. Medina, M. V. Matz, Novel polymorphic microsatellite markers for population genetics of the endangered Caribbean star coral, *Montastraea faveolata*. *Mar. Biodivers.* **43**, 167–172 (2013).
56. S. Wang, E. Meyer, J. K. McKay, M. V. Matz, 2b-RAD: A simple and flexible method for genome-wide genotyping. *Nat. Methods* **9**, 808–810 (2012).
57. M. Martin, Cutadapt removes adapter sequences from high-throughput sequencing reads. *EMBnet J.* **17**, 10–12 (2011).
58. M. Aranda, Y. Li, Y. J. Liew, S. Baumgarten, O. Simakov, M. C. Wilson, J. Piel, H. Ashoor, S. Bougouffa, V. B. Bajic, T. Ryu, T. Ravasi, T. Bayer, G. Mickle, H. Kim, J. Bhak,

- T. C. Lajeunesse, C. R. Voolstra, Genomes of coral dinoflagellate symbionts highlight evolutionary adaptations conducive to a symbiotic lifestyle. *Sci. Rep.* **6**, 39734 (2016).
59. E. Shoguchi, C. Shinzato, T. Kawashima, F. Gyoja, S. Mungpakdee, R. Koyanagi, T. Takeuchi, K. Hisata, M. Tanaka, M. Fujiwara, M. Hamada, A. Seidi, M. Fujie, T. Usami, H. Goto, S. Yamasaki, N. Arakaki, Y. Suzuki, S. Sugano, A. Toyoda, Y. Kuroki, A. Fujiyama, M. Medina, M. A. Coffroth, D. Bhattacharya, N. Satoh, Draft assembly of the *Symbiodinium minutum* nuclear genome reveals dinoflagellate gene structure. *Curr. Biol.* **23**, 1399–1408 (2013).
60. H. Liu, T. G. Stephens, R. A. González-Pech, V. H. Beltran, B. Lapeyre, P. Bongaerts, I. Cooke, M. Aranda, D. G. Bourne, S. Forêt, D. J. Miller, M. J. H. van Oppen, C. R. Voolstra, M. A. Ragan, C. X. Chan, *Symbiodinium* genomes reveal adaptive evolution of functions related to coral–dinoflagellate symbiosis. *Commun. Biol.* **1**, 95 (2018).
61. K. E. Dougan, “A comparative genomics exploration of inter-partner metabolic signaling in the coral–algal symbiosis,” thesis, Florida International University, Miami, FL (2020).
62. B. Langmead, S. L. Salzberg, Fast gapped-read alignment with Bowtie 2. *Nat. Methods* **9**, 357–359 (2012).
63. L. Fu, B. Niu, Z. Zhu, S. Wu, W. Li, CD-HIT: Accelerated for clustering the next-generation sequencing data. *Bioinformatics* **28**, 3150–3152 (2012).
64. T. S. Korneliussen, A. Albrechtsen, R. Nielsen, ANGSD: Analysis of next generation sequencing data. *BMC Bioinformatics* **15**, 356 (2014).
65. R Core Team, R: A language and environment for statistical computing (R Foundation for Statistical Computing, 2022); <https://R-project.org/>.
66. J. Oksanen, G. L. Simpson, F. G. Blanchet, R. Kindt, P. Legendre, P. R. Minchin, R. B. O’Hara, P. Solymos, M. H. H. Stevens, E. Szoecs, H. Wagner, M. Barbour, M. Bedward, B. Bolker, D. Borcard, G. Carvalho, M. Chirico, M. D. Caceres, S. Durand, H. B. A. Evangelista, R. FitzJohn, M. Friendly, B. Furneaux, G. Hannigan, M. O. Hill, L. Lahti, D. McGlenn, M.-H. Ouellette, E. R. Cunha, T. Smith, A. Stier, C. J. F. T. Braak, J. Weedon, vegan: Community Ecology Package, version 2.6-2 (2022); <https://CRAN.R-project.org/package=vegan>.
67. L. Skotte, T. S. Korneliussen, A. Albrechtsen, Estimating individual admixture proportions from next generation sequencing data. *Genetics* **195**, 693–702 (2013).
68. T. S. Korneliussen, I. Moltke, NgsRelate: A software tool for estimating pairwise relatedness from next-generation sequencing data. *Bioinformatics* **31**, 4009–4011 (2015).
69. A. Apprill, S. McNally, R. Parsons, L. Weber, Minor revision to V4 region SSU rRNA 806R gene primer greatly increases detection of SAR11 bacterioplankton. *Aquat. Microb. Ecol.* **75**, 129–137 (2015).
70. A. E. Parada, D. M. Needham, J. A. Fuhrman, Every base matters: Assessing small subunit rRNA primers for marine microbiomes with mock communities, time series and global field samples. *Environ. Microbiol.* **18**, 1403–1414 (2016).
71. B. Hume, C. D’Angelo, J. Burt, A. C. Baker, B. Riegl, J. Wiedenmann, Corals from the Persian/Arabian Gulf as models for thermotolerant reef-builders: Prevalence of clade C3 *Symbiodinium*, host fluorescence and ex situ temperature tolerance. *Mar. Pollut. Bull.* **72**, 313–322 (2013).
72. B. C. C. Hume, C. D’Angelo, E. G. Smith, J. R. Stevens, J. Burt, J. Wiedenmann, *Symbiodinium thermophilum* sp. nov., a thermotolerant symbiotic alga prevalent in corals of the world’s hottest sea, the Persian/Arabian Gulf. *Sci. Rep.* **5**, 8562 (2015).
73. B. J. Callahan, P. J. McMurdie, M. J. Rosen, A. W. Han, A. J. A. Johnson, S. P. Holmes, DADA2: High-resolution sample inference from Illumina amplicon data. *Nat. Methods* **13**, 581–583 (2016).
74. C. Quast, E. Pruesse, P. Yilmaz, J. Gerken, T. Schweer, P. Yarza, J. Peplies, F. O. Glöckner, The SILVA ribosomal RNA gene database project: Improved data processing and web-based tools. *Nucleic Acids Res.* **41**, D590–D596 (2012).
75. C. Camacho, G. Coulouris, V. Avagyan, N. Ma, J. Papadopoulos, K. Bealer, T. L. Madden, BLAST+: Architecture and applications. *BMC Bioinformatics* **10**, 421 (2009).
76. P. J. McMurdie, S. Holmes, phyloseq: An R package for reproducible interactive analysis and graphics of microbiome census data. *PLOS ONE* **8**, e61217 (2013).
77. A. M. Rodas, R. M. Wright, L. K. Buie, H. E. Aichelman, K. D. Castillo, S. W. Davies, Eukaryotic plankton communities across reef environments in Bocas del Toro Archipelago, Panamá. *Coral Reefs* **39**, 1453–1467 (2020).
78. M. M. Bradford, A rapid and sensitive method for the quantitation of microgram quantities of protein utilizing the principle of protein–dye binding. *Anal. Biochem.* **72**, 248–254 (1976).
79. T. Masuko, A. Minami, N. Iwasaki, T. Majima, S.-I. Nishimura, Y. C. Lee, Carbohydrate analysis by a phenol–sulfuric acid method in microplate format. *Anal. Biochem.* **339**, 69–72 (2005).
80. M. S. Burriesci, T. K. Raab, J. R. Pringle, Evidence that glucose is the major transferred metabolite in dinoflagellate–cnidarian symbiosis. *J. Exp. Biol.* **215**, 3467–3477 (2012).
81. L. J. Rodrigues, A. G. Grotto, Energy reserves and metabolism as indicators of coral recovery from bleaching. *Limnol. Oceanogr.* **52**, 1874–1882 (2007).
82. S. W. Jeffrey, F. Haxo, Photosynthetic pigments of symbiotic dinoflagellates (Zooxanthellae) from corals and clams. *Biol. Bull.* **135**, 149–165 (1968).
83. I. E. Conti-Jerpe, P. D. Thompson, C. W. M. Wong, N. L. Oliveira, N. N. Duprey, M. A. Moynihan, D. M. Baker, Trophic strategy and bleaching resistance in reef-building corals. *Sci. Adv.* **6**, eaaz5443 (2020).
84. C. A. Schneider, W. S. Rasband, K. W. Eliceiri, NIH Image to ImageJ: 25 years of image analysis. *Nat. Methods* **9**, 671–675 (2012).
85. S. Enriquez, E. R. Méndez, R. Iglesias-Prieto, Multiple scattering on coral skeletons enhances light absorption by symbiotic algae. *Limnol. Oceanogr.* **50**, 1025–1032 (2005).
86. E. Terán, E. R. Méndez, S. Enriquez, R. Iglesias-Prieto, Multiple light scattering and absorption in reef-building corals. *Appl. Optics* **49**, 5032–5042 (2010).
87. U. E. Siebeck, N. J. Marshall, A. Klüter, O. Hoegh-Guldberg, Monitoring coral bleaching using a colour reference card. *Coral Reefs* **25**, 453–460 (2006).
88. J. P. Rippe, J. H. Baumann, D. N. De Leener, H. E. Aichelman, E. B. Friedlander, S. W. Davies, K. D. Castillo, Corals sustain growth but not skeletal density across the Florida Keys Reef Tract despite ongoing warming. *Glob. Chang. Biol.* **24**, 5205–5217 (2018).
89. T. M. DeCarlo, A. L. Cohen, H. C. Barkley, Q. Cobban, C. Young, K. E. Shamberger, R. E. Brainard, Y. Golbuu, Coral macrobioerosion is accelerated by ocean acidification and nutrients. *Geology* **43**, 7–10 (2015).
90. N. A. Rayner, D. E. Parker, E. B. Horton, C. K. Folland, L. V. Alexander, D. P. Rowell, E. C. Kent, A. Kaplan, Global analyses of sea surface temperature, sea ice, and night marine air temperature since the late nineteenth century. *J. Geophys. Res. Atmos.* **108**, 4407 (2003).
91. C. B. Bove, L. Mudge, J. F. Bruno, A century of warming on Caribbean reefs. *PLOS Clim.* **1**, e0000002 (2022).
92. Q. Peng, S.-P. Xie, D. Wang, R. X. Huang, G. Chen, Y. Shu, J.-R. Shi, W. Liu, Surface warming–induced global acceleration of upper ocean currents. *Sci. Adv.* **8**, eabj8394 (2022).

Acknowledgments: We extend appreciation to the staff at the Smithsonian Tropical Research Institute at Bocas del Toro, especially U. Gonzalez for assistance in coordinating field work. We thank our fearless boat captain S. Castillo, in addition to C. Fieseler and L. Buie for field assistance. We also thank J. Weldon for assistance with physiology assays and M. Powell for assistance with sampling DNA from coral cores. Analysis was made possible through BU’s Shared Computing Cluster. **Funding:** This work was supported by a National Science Foundation grant (OCE-1459522 to K.D.C. and S.W.D.); a National Academies of Sciences, Engineering, and Medicine Gulf Research Program Fellowship (to S.W.D.); Boston University start-up funds (to S.W.D.); a National Science Foundation Graduate Research Fellowship (to H.E.A.); the Boston University Marion Kramer Award (to H.E.A.); the Boston University Marine Program (S.W.D. and H.E.A.); and the Boston University Undergraduate Research Opportunities Program (A.M.P., L.T., and O.C.N.). **Author contributions:** Conceptualization: S.W.D., K.D.C., and H.E.A. Methodology: P.G., B.E.B., S.W.D., H.E.A., J.H.B., J.P.R., and K.D.C. Investigation: H.E.A., B.E.B., K.G.-C., M.I.M.-R., L.T., O.C.N., D.S., A.M.P., N.G.K., J.E.F., C.B.B., and A.M.H. Visualization: H.E.A. Supervision: H.E.A., S.W.D., and K.D.C. Writing—original draft: H.E.A. and S.W.D. Writing—review and editing: H.E.A., B.E.B., K.G.-C., M.I.M.-R., J.E.F., L.T., A.M.H., C.B.B., O.C.N., A.M.P., D.S., N.G.K., J.H.B., J.P.R., P.G., K.D.C., and S.W.D. **Competing interests:** The authors declare that they have no competing interests. **Data and materials availability:** All data needed to evaluate the conclusions in the paper are present in the paper and/or the Supplementary Materials. Raw sequencing data are available on NCBI’s SRA (2bRAD BioProject ID=PRJNA973074, 16S/ITS2 BioProject ID=PRJNA973086). All other data, code, and materials needed to evaluate the conclusions in the paper can be found in the Github repository associated with this project (<https://github.com/hannahaichelman/CrypticCorals>) and are additionally hosted on Zenodo (DOI: 10.5281/zenodo.13963677).

Submitted 9 July 2024
Accepted 13 December 2024
Published 15 January 2025
10.1126/sciadv.adr5237